

Additive Manufacturing-Enabled Architected Nanocomposite Lattices Coated with Plasmonic Nanoparticles for Water Pollutants Detection

Sara Fateixa,* Marc Landauer, Johannes Schneider, Shanmugam Kumar,* and Robert Böhm

Novel low-cost materials to uptake and detect vestigial amounts of pesticides are highly desirable for water quality monitoring. Herein, are demonstrated, for the first time, surface-enhanced Raman scattering (SERS) sensors enabled via additively manufactured lattices coated with plasmonic nanoparticles (NPs) for detecting pesticides in real water samples. The architected lattices comprising polypropylene (PP) and multiwall carbon nanotubes (MWCNTs) are realized via fused filament fabrication (FFF). In the first stage, the SERS performance of the PP/MWCNT filaments coated with distinct metallic NPs (Ag NPs and Au NPs) is evaluated using methylene blue (MB) as molecular probe. Thereafter, distinctly architected hybrid SERS sensors with periodic porous and fully dense geometries are investigated as adsorbents to uptake MB from aqueous solutions and subsequent detection using SERS. The spatial distribution of MB and Ag NPs on the FFF-printed lattices is accomplished by SERS imaging. The best hybrid composite is used as SERS probing system to detect low amounts of pesticides (thiram and paraquat) and offers a detection limit of 100 nM for both pesticides. As a proof-of-concept, FFF-enabled test strips are used to detect in loco paraquat molecules spiked on real water samples (Estuary Aveiro water and tap water) using a portable Raman spectrometer.

1. Introduction

Water pollution is a global challenge that has increased in both developed and developing countries, discouraging economic growth and decreasing the physical and environmental health of billions of people. According to the World Health Organization, pesticides are a broad spectrum of chemical and organic mixtures used in agriculture to protect fruits and cereals from plagues and preserve them in crops, transportation and storage.^[1] The overuse of these pesticides affects the plants and animals of the whole ecological structure and contaminates soils, groundwater and seawater.^[1–3] This type of residue, even in low concentrations, represents a severe risk to human health.^[4] Therefore, it is essential to develop methods to detect the smallest amounts of a substance in water in a user-friendly, inexpensive, and reliable way. Currently, high-performance liquid chromatography,^[5,6] gas chromatography, and mass spectrometry^[7,8] are the most


employed methods for detecting pollutants; however, these methods are expensive and time-consuming. Furthermore, they require trained staff and sample manipulation or preparation. Therefore, surface-enhanced Raman scattering (SERS) spectroscopy has been used over the last decade as a good alternative technique to detect low amounts of pesticides in water samples.^[9–13]

SERS is a non-destructive vibrational technique that detects vestigial amounts of molecules of interest using nanostructured materials based on plasmonic particles, such as gold and silver nanoparticles (Au NPs and Ag NPs).^[14,15] These plasmonic structures play an important role in the successful application of SERS since the interaction between the molecules adsorbed on the surface of these plasmonic structures will significantly enhance the Raman signal of the molecular probe and, consequently, its detection. However, pesticide compounds in real water samples are usually in low concentrations. An interesting alternative involves the uptake of the pesticide molecules by a sorbent material that allows pre-concentration procedures and acts as a SERS sensor for optical detection. Following this line, Fateixa et al. have reported the fabrication of plasmonic

S. Fateixa
Department of Chemistry, CICECO Aveiro Institute of Materials
University of Aveiro
Aveiro 3810-193, Portugal
E-mail: sarafateixa@ua.pt

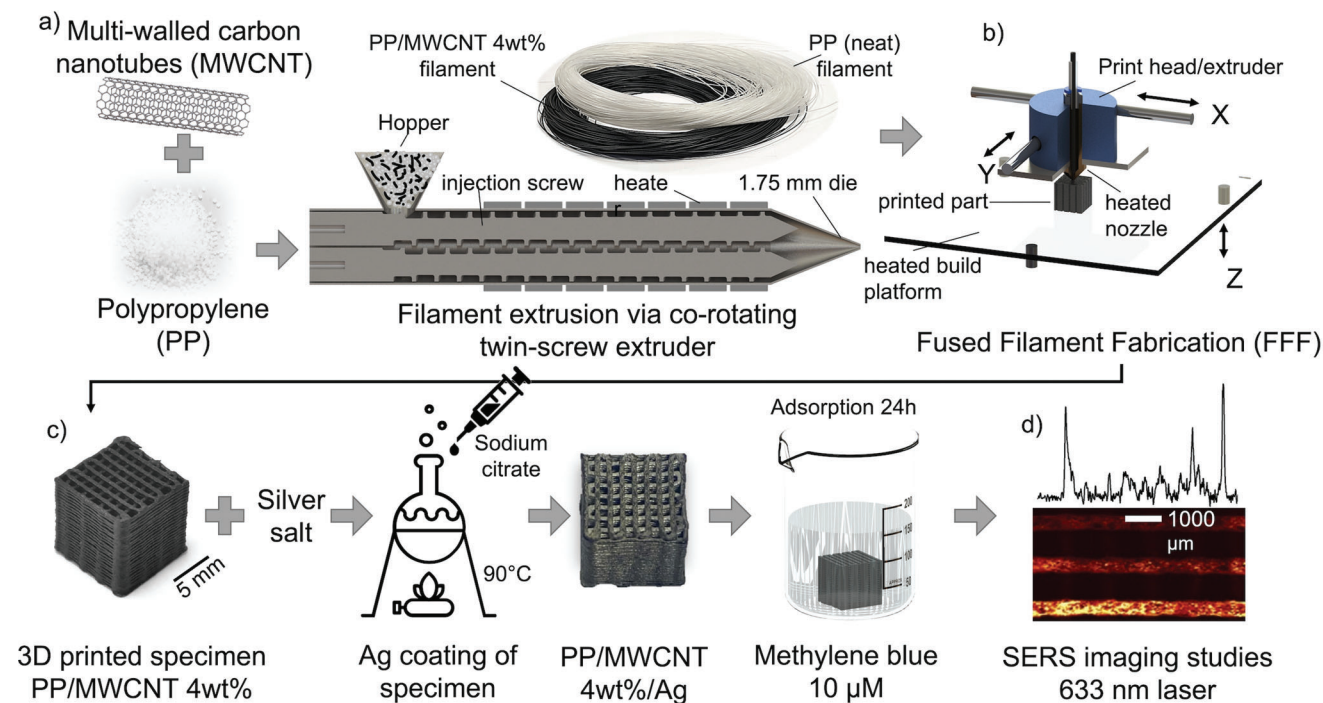
M. Landauer, R. Böhm
Faculty of Engineering
HTWK Leipzig
PF 30 11 66, 04251 Leipzig, Germany

J. Schneider, S. Kumar
James Watt School of Engineering
University of Glasgow
Glasgow G12 8LT, UK
E-mail: msv.kumar@glasgow.ac.uk

 The ORCID identification number(s) for the author(s) of this article can be found under <https://doi.org/10.1002/mame.202300060>

© 2023 The Authors. Macromolecular Materials and Engineering published by Wiley-VCH GmbH. This is an open access article under the terms of the Creative Commons Attribution License, which permits use, distribution and reproduction in any medium, provided the original work is properly cited.

DOI: 10.1002/mame.202300060



Scheme 1. Processing of PP/MWCNT nanocomposites and coating them with plasmonic NPs: a) nanoengineered filament development via melt-blending, b) additive manufacturing of 3D cellular architectures via FFF, c) coating cellular architectures with Ag NPs, and d) SERS imaging detection of organic dyes in water samples.

structures for the capture and optical detection of water pollutants, including magnetic sensors^[16,17] and Ag NPs dispersed in vectran^[10] and polyamide^[18] filter membranes.

In recent years, there has been significant interest in exploring SERS platforms for water pollutants detection by integrating plasmonic metals into multifunctional hybrid nanostructures. However, research on hybrid SERS sensors based on 3D printed cellular architectures has been less explored despite their potential to uptake and detect molecular probes.^[19–21] This study, therefore, is focused on additive manufacturing (AM)-enabled polymer nanocomposite lattices coated with plasmonic NPs for water pollutants detection.

AM (also known as 3D printing) has become increasingly popular due to its various advantages compared to traditional manufacturing techniques.^[22–25] It opens new possibilities to quickly produce prototypes, customized products and complex geometries such as cellular architectures from different families of materials at different length scales.^[26] AM can be broadly grouped into liquid-, solid-, and powder-based processes,^[27] with fused filament fabrication (FFF) being the most widely used process today, as it is easily accessible and cost-effective. Moreover, FFF requires little initial investment and produces little waste during the manufacturing process.^[27–32] FFF enables the production of a wide range of thermoplastic materials, including polypropylene (PP). PP has pronounced biocompatibility and is extensively used in an array of applications, including the automotive and textiles industries.^[33] At the same time, PP is not yet widely used in AM due to issues, such as severe warping and laxity of adhesion of the part to print-bed encountered during 3D printing.^[34–36] Nano-fillers, such as metal NPs, carbon nanotubes (CNTs), and

graphene nanoplatelets (GNPs) are incorporated into PP to create multifunctional nanocomposites. The addition of electrically conductive fillers to the PP matrix, besides enhancing the mechanical properties (such as strength, stiffness, and toughness) of the resulting nanocomposites, enables in situ structural health monitoring, offering great potential for developing smart materials and systems.^[25,29,37]

This work aims to develop AM-enabled hybrid SERS sensor for pesticide detection in real water samples. We realized periodic cellular nanocomposite architectures and fully dense nanocomposites via FFF technique by incorporating multi-walled carbon nanotubes (MWCNTs) into PP matrix. The 3D printed periodic cellular structures, known as lattices, were coated with Ag NPs, envisaging their use for the uptake and SERS detection of vestigial amounts of organic dyes in water, namely methylene blue (MB) (**Scheme 1**). As a proof of concept, we demonstrate the performance of FFF-enabled test strip in detecting in loco low amounts of pesticides spiked on real water samples such as Estuary Aveiro water and tap water using a portable Raman spectrometer. Still, this methodology can be extended to other pesticides or bioanalytes.

2. Experimental Section

2.1. Materials

The following materials and chemicals were used as purchased: PP random copolymer (RA140E, Borouge Pte. Ltd.), MWCNTs (with a diameter of $\approx 10\text{--}12$ nm and length > 30 μm), were supplied by Applied Nanostructured Solution, LLC),

hydrogen tetrachloroaurate (III) trihydrate (HAuCl₄·3H₂O, 99.9%, Sigma-Aldrich), silver nitrate (AgNO₃, 99.9%, J. M. Vaz Pereira), trisodium citrate dihydrate (Na₃C₆H₅O₇·2H₂O, 99%, Sigma-Aldrich), MB (C₁₆H₁₈N₃SCl, Riedel-De Haen), thiram (C₆H₁₂N₂S₄, Sigma-Aldrich); paraquat (C₁₂H₁₄C₁₂N₂, >98%, Sigma-Aldrich), and ethanol absolute anhydrous (CH₂CH₃OH, VWR). Ultrapure water (18.2 MΩ·cm, 25 °C, MilliQ, Millipore) was used to prepare metallic colloids and aqueous solutions of analytes. Aveiro Estuary and tap water had local origins and were used as analytical samples after adding paraquat in the laboratory.

2.2. Preparation of Filaments via Melt-Blending for Fused Filaments Fabrication

The filaments were produced as described in the authors' previous study^[33] via melt-blending technique using a co-rotating twin-screw extruder, Coperion ZSK 18, Germany, with the screws having a length to diameter ratio of 40. The heating zones' temperatures were set between 170 and 220 °C, while the screw speed was set at 220 rpm for extruding the filament with a target diameter of 1.75 mm. Detailed processing settings, including raw material characterization, could be found in authors' previous publication,^[33] focusing on the synthesis and characteristics of CNT incorporated, AM-enabled thermoplastic nanocomposites.

2.3. Additive Manufacturing of Architected and Bulk Composites via FFF

The specimens used in this study were produced using the FFF 3D printing process, in which thermoplastic filament was transported from a spool to a print head where it was fused and then extruded through a nozzle attached to the print head to build the part layer by layer on a build plate, according to the sliced CAD (Computer Aided Design) model. The printing temperature was set to 220 °C, the bed temperature to 120 °C, layer height to 0.2 mm, and the printing speed to 900 mm min⁻¹. The prints were fabricated using Apium P220 (Apium Additive Technologies GmbH, Germany) FFF 3D printer. The non-porous and cellular geometries with an overall size of 10 × 10 × 10 mm³ (Figure S1, Supporting Information) were 3D printed. The cellular architecture was designed such that each layer could be printed in one single nozzle movement, allowing a very precise material deposition. The extrusion width was set to 0.45 mm, resulting in gaps between the individual beads of ≈0.73 mm. The resulting relative density, a measure of solid volume of the cellular material was $\bar{\rho} = 56\%$. Conversely, engineered porosity of the cellular material, $\bar{\phi} = (1 - \bar{\rho}) = 44\%$. The surface area density was calculated for periodic cellular architectures and fully dense samples and the values are presented in **Table 1**.

A unique design was developed for portal Raman to be compatible with existing devices. The setup consisted of a two-part assembly, the test stripe base plate, and the test stripe insert (Figure S2, Supporting Information). The test stripe base plate, measuring 2.3 mm × 9.8 mm × 24.8 mm, was manufactured using digital light processing AM technique, in which a photopolymer was cured layer by layer within a resin tank. As there were no specific requirements to the base plate other than holding the test stripe insert, PlasGray, a photopolymer, was used for

Table 1. Values for volume, surface area, and surface area density for periodic cellular and fully dense structure samples.

	Periodic cellular	Full dense
Volume (mm ³)	557.09	1000
Surface area (mm ²)	4187.54	600
Surface area density (mm ² mm ⁻³)	7.5	0.6
Surface area density (m ⁻¹)	7516.8	600
Ratio of surface area density: cellular/full dense	12.5	

Table 2. Metal NP content in the filaments and 3D samples by ICP.

Sample	Ag content [mg kg ⁻¹]	Au content [mg kg ⁻¹]
Ag/PP filament	1010	—
Ag/PP4% filament	988	—
Au/PP filament	—	335
Au/PP4% filament	—	1555
3D Ag/PP4% solid	535	—
3D Ag/PP4% cellular	488	—

printing, allowing a much higher printing resolution than what could be achieved via FFF. The test stripe inserts, measuring 8 mm × 8 mm × 0.8 mm, had a cylindrical recess and were manufactured via FFF using PP4%. The recess allowed carrying the water drop to be analyzed by Raman spectroscopy.

2.4. In Situ Metallic Coating of PP/PP4% Filaments and 3D-Printed PP/PP4% Composites

The in situ metallic coating of PP and PP4% filaments and 3D-printed composites was performed by employing the citrate reduction method for the synthesis of colloidal Ag and Au NPs^[38] but in the presence of filaments (150 mg) or 3D composite (150 mg). Briefly, 100 mL of 2 mM AgNO₃ (Ag coating) or 1 mM HAuCl₄·3H₂O (Au coating) was boiled (95 °C) under reflux and vigorous stirring for 10 min. Then 3 mL of sodium citrate solution (1% w/v) was added dropwise to the boiling solution. The mixture was then refluxed for more 45 min and slowly cooled at room temperature. The resulting composites were isolated by filtration, washed three times with distilled water, and dried overnight in an incubator at 40 °C. The metal content in the filaments and 3D samples was evaluated by inductively coupled plasma (ICP) (**Table 2**).

2.5. Adsorption Experiments of MB onto 3D Lattices

The amount of adsorbed MB on to the 3D printed lattices was determined by the interpolation of UV absorption of the supernatant at 663 nm. The performance of each 3D printed sample fabricated with PP and PP4% (with and without Ag NPs) was investigated for the same MB concentration (10 μM) at pH 9, with 10 min, 2, and 24 h contact times. The pH of the MB aqueous solution was adjusted to the required value by adding NaOH.

First, the 3D architectures were emerged in ultrapure water overnight to eliminate the possible lixiviation of the Ag NPs of

the materials' surface. Then, 10 mL of MB aqueous solution was added to one piece of each 3D printed sample. These mixtures were then incubated using a mini rotor at room temperature, and an aliquot of 1 mL was taken for each contact time. Each aliquot was centrifuged for 5 min at 13 000 rpm and analyzed by UV–VIS spectroscopy. Three replicas for each 3D printed sample were performed.

2.6. SERS Measurements and Raman Imaging

The PP4% filaments and 3D-printed composites (cellular and non-porous structure and portable Raman assay) were investigated as SERS platforms to detect water pollutants (MB, thiram e paraquat) in real water samples. Raman spectra and images were acquired using a Raman-AFM-SNOM WITec alpha 300RAS⁺ confocal spectrometer. A He:Ne laser operating at 633 nm was used as the excitation source. Pure PP and PP4% without metallic NPs were used in control samples for all the SERS measurements. The SERS measurements were performed in three replicas in different areas of the filaments and composites to check the reproducibility of the measurements.

The sensitivity of the PP and PP4% filaments coated with metallic NPs as SERS platforms was evaluated using MB as a molecular probe. 10 μ L of a 10 μ M MB aqueous solution was dropped on substrates, taped on a glass slide, and dried in air. Ten spectra were acquired (10 acquisitions, 2 s each) on each filament, and an average Raman spectrum was obtained using WITec software (Project 5.3⁺).

High-resolution Raman images of MB adsorbed on Ag/PP4% and Au/PP4% filaments were performed by taking 150 \times 150 Raman spectra (in total 22 500 spectra) in an area of 50 μ m \times 50 μ m with the integration time for each spectrum set as 0.05 s (0.1 mW of laser power; 100 \times objective). Large Raman images on MB adsorbed on 3D_Ag/PP4%cell and 3D_Ag/PP4%non architectures were achieved by taking 200 \times 200 Raman spectra (in total 40 000 spectra) in an area of 6 \times 6 mm with the integration time for each spectrum set as 0.05 s (0.1 mW of laser power; 10 \times objective). Raman images were constructed by integrating the absolute area underneath the MB Raman band at 1620 cm^{-1} (assigned to the $\nu(\text{CC}) + \delta(\text{CH})$ in plane (ring), $\nu(\text{CN}) + \nu(\text{CC})$) using WITec software (Project 5.3⁺).

To detect the pesticides thiram and paraquat, all samples were prepared using personnel protective equipment in a fume hood. In the case of thiram samples in solution, an ethanolic stock solution of thiram with a concentration of 1 mM was first prepared. So, thiram and paraquat aqueous solutions (1 mM) were used to prepare diluted samples, with concentrations between 100 μ M and 100 nM in ultrapure water to evaluate the SERS sensitivity and selectivity of the Ag/PP and Ag/PP4% filaments. The experimental detection limit of pesticides was considered the lowest concentration for which a Raman signal was distinct from the background noise. The signal-to-noise ratio was calculated using the average peak height of the Raman band (S) obtained from four spectra divided by the square root of the standard deviation of the peak height (σ_y).^[39]

Raman imaging took 150 \times 150 Raman spectra in a uniform 30 \times 30 μ m grid. A 100 \times objective was used, and the integration time for each spectrum was 0.1 s. Raman images were constructed by

integrating the absolute area underneath the thiram Raman band at 1380 cm^{-1} (assigned to the $\nu(\text{C-N})$ coupled to $\delta_{\text{sym}}(\text{CH}_3)$) and paraquat Raman band at 841 cm^{-1} (assigned to the $\nu(\text{C-N})$) using WITec software (Project 5.3⁺). To compare the SERS sensitivity between different substrates, 20 spectra were extracted from the brighter yellow areas of the Raman map (areas showing the strongest SERS signal of the chosen band) of each substrate, and an average Raman spectrum was obtained for each substrate using WITec software.

2.7. SERS Measurements in Real Samples Using Portable Raman Spectrometer

For the detection of paraquat in real samples spiked with paraquat, an aqueous solution of the herbicide (1 mM) was prepared in Aveiro Estuary water (seawater) and tap water and diluted from 1 mM to 100 nM. The diluted paraquat solutions were dropped in the center of the 3D printed portable Raman assay (Ag/PP4%) and let dry at room temperature. The samples were analyzed with a portable Raman spectrometer (Module C13560) with a 785 nm laser source. Each Raman spectrum was acquired with ten acquisitions, 1000 s each acquisition. For each paraquat concentration, two test stripes were tested.

2.8. Instrumentation

Scanning electron microscopy (SEM) images were obtained with a SU-70 Hitachi instrument fitted with an energy dispersive spectroscopy (EDS) accessory (EDS detector: Bruker AXS; software: Quantax), operated at 15 kV. Samples for SEM were placed on carbon tape and coated with carbon before the analysis in secondary electron (SE) and back-scattered electron (BSE) modes. A Hitachi HD-2700 STEM microscope operating at 200 kV was employed to collect the transmission electron microscopy (TEM) images of the metallic colloids on carbon-coated Cu grids. The XRD data were collected using a PAN analytical Empyrean X-ray diffractometer (PANanalytical, Almelo, The Netherlands) equipped with Cu K. The XRD data were collected using the filament on a silicon holder. The optical measurements were recorded using a Jasco V-780 spectrophotometer. For the filaments and 3D-printed composites, the spectra were recorded in the diffuse reflectance mode using MgO as a reference. The corresponding absorption spectra were obtained by applying the Kubelka–Munk function to the experimental reflectance spectra. Raman and atomic force microscopy (AFM) studies were carried out on a Raman-AFM-SNOM WITec alpha 300RAS⁺. For the Raman studies, a He:Ne laser operating at 633 nm was used as the excitation source with power set at 0.1 mW. The AFM measurements were carried out in tapping mode (AC-AFM) using a tip-cantilever silicon reflex-coated with a spring constant of $k = 2.8 \text{ N m}^{-1}$ and 75 kHz of resonance frequency. The scanning image was 5 μ m \times 5 μ m (512 points per line \times 512 lines per image) with a scan speed of 1 s/line and 1 μ m \times 1 μ m (256 points per line \times 256 lines per image) with a scan speed of 1 s/line (both with the same retrace speed). The SERS analysis using a portable Raman spectrometer was accomplished using a portable Raman spectroscopic module C13560 from Hamamatsu Photon Business with an excitation source operating at 785 nm with power

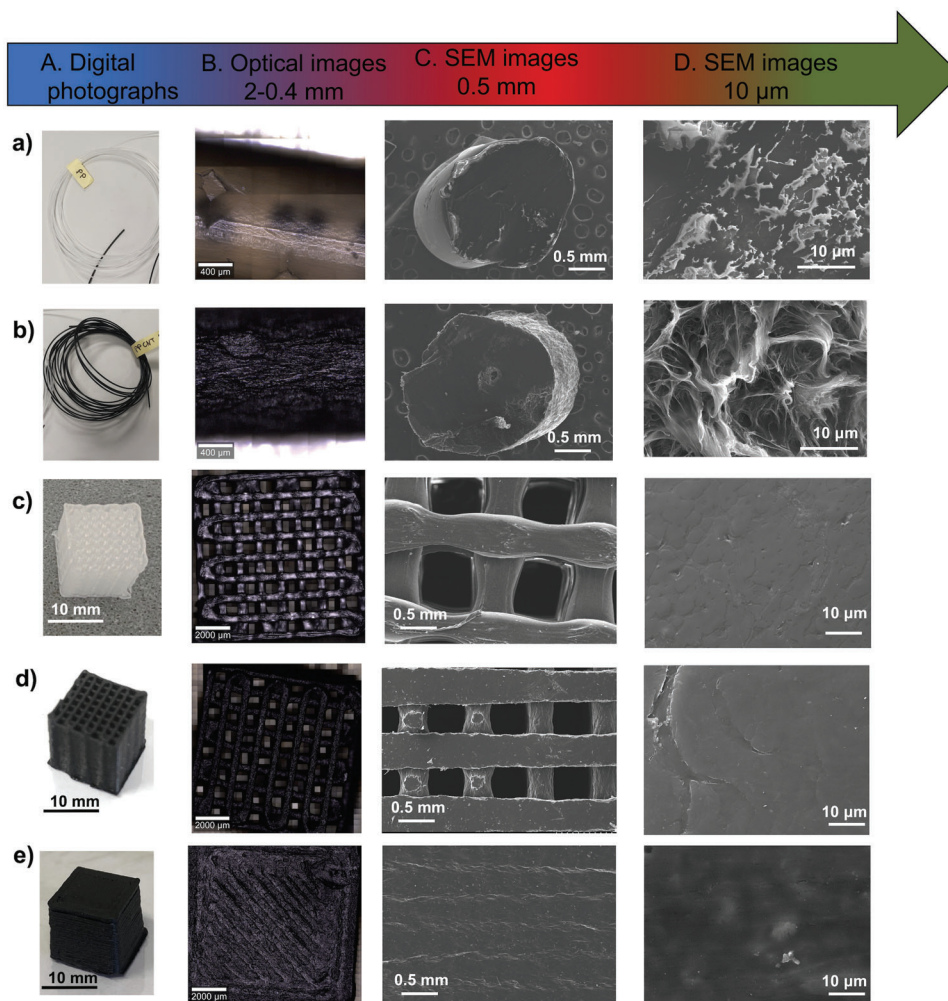


Figure 1. A) Digital photographs of PP (a) and PP4% (b) filaments and 3D printed composites: 3D_PPcell (c), 3D_PP4%cell (d), and 3D_PP4%non (e). B) Optical images of the filaments and 3D printed lattice (2–0.4 mm). C) SEM images showing the cross section of filaments (a,b) and the surface of the 3D printed lattice (c–e) (10 μm). D) Higher resolution SEM images.

set at 1 mW. The ICP-optical emission spectroscopy analysis was carried out using a Jobin Yvon Activa M equipment. Zeta potential measurement was performed using a Zetasizer Nanoseries instrument from Malvern Instruments. Nitrogen physisorption experiments were performed with a Gemini V2.0 Micromeritics Instrument to investigate the textural properties of the carbonaceous materials. The specific surface area of the materials was determined from N_2 adsorption/desorption isotherms using the Brunauer–Emmett–Teller equation.^[40]

3. Results and Discussion

3.1. Additive Manufacturing of Cellular and Fully Dense Nanocomposites via FFF

CNTs are well-known for their thermal, electrical, and mechanical properties, making them an appropriate candidate for incorporating into 3D printable polymers. MWCNTs possess structural defects that provide suitable nucleation sites, allowing for strong interactions with polymers, cross-linking, and

functionalization.^[41] From previous work, we note that the addition of 4 wt% of MWCNT to neat PP enhanced the crystallinity and increased the stiffness and strength properties of AM-enabled nanoengineered PP/MWCNT composites.^[33] Following this work, PP filaments with 4 wt% of MWCNT (PP4%) were prepared by melt-blending and used to realize periodic cellular and fully dense nanocomposites. **Figure 1** shows the morphology and surface roughness of PP and PP4% filaments and the 3D printed lattices of PP and PP4% (3D_PPcell; 3D_PP4%cell) as well as 3D printed non-porous (fully dense or bulk) architectures of PP4% (3D_PP4%non) characterized by optical and scanning electron microscopy (SEM).

Incorporating 4 wt% of MWCNT into a neat PP matrix changed not only the properties of the filament but also its color (black coloration, Figure 1A[b,d]). The optical images for PP and PP4% presented in Figure 1B[a,b] seem quite different, suggesting a more rough surface of the PP4% filaments due to the MWCNTs on the PP matrix. The surface roughness of the filaments was analyzed by AFM, and the results are presented in Figure S3a,b, Supporting Information. The average surface roughness

value (root mean square [RMS]) for PP is 27,3 and 24,9 for PP4% filaments. This result shows that the reinforcement of neat PP with MWCNT does not change the roughness of the filament's surface, resulting in a uniform dispersion of MWCNTs in the PP matrix. In addition, the high-resolution AFM image acquired on the PP4% filaments shows MWCNTs on the filament's surface with a diameter of 40 nm (Figure S3c, Supporting Information). This value is in line with the values reported in the literature for MWCNTs. This data is extremely important because the presence of MWCNTs on the filament surface is vital to a better metallic coating of the filaments and, consequently, a better SERS performance of the hybrid sensor.

To get more insights into the dispersion of the MWCNTs in the filament, a cross section of the filament was analyzed by SEM (Figure 1C[b],D[b]). The presence of individual MWCNTs or small CNT bundles dispersed in the PP matrix can be seen in Figure 1D[b]. By contrast, the PP filament cross section illustrated in Figure 1D[a] shows a very smooth surface with a compact matrix.

Digital photographs of the PP and PP4% architected cellular structures and PP4% solid structure of $10 \times 10 \times 10 \text{ mm}^3$ are shown in Figure 1A[c–e], respectively. While the optical image of the 3D cubic non-porous sample shows no spacing between the filament extrusions on the top of the structure (Figure 1B[e]), the 3D cubic cellular network shows a well-ordered pattern of deposited polymer with a width of $\approx 0.45 \text{ mm}$ and gaps of 0.73 mm width (Figure 1B[c,d]). The SEM analysis of the printed samples shows that the printing process does not induce defects or aggregation on the filaments, revealing a smooth surface similar to the filament (Figure 1C[c,d]).

The neat PP and PP4% filaments were characterized by Raman spectroscopy (Figure S4, Supporting Information). The main Raman bands of neat PP are observed at their regular positions and are assigned according to the literature (Table S1, Supporting Information).^[42] The symmetric CH_2 and CH_3 stretching modes of PP at 2840 and 2885 cm^{-1} , respectively, indicate PP crystallinity.^[43] If the band's intensity at 2840 cm^{-1} is lower than the band at 2885 cm^{-1} , the PP has high crystallinity. In the case of PP filaments reinforced with 4% wt of MWCNTs, the Raman spectrum is dominated by the characteristic Raman features for carbon materials: the D band (disorder band) at 1345 cm^{-1} assigned to the sp^3 -carbon containing moieties due to the defects introduced to the graphene lattice, the G band at 1568 cm^{-1} assigned to the sp^2 carbons of the 2D hexagonal lattice (graphite band), and the G' band at 2676 cm^{-1} assigned to the second order overtone. These results are in good agreement with reports in the literature for MWCNTs.^[44,45] Beside the Raman bands of MWCNTs, it can be observed some bands obtained for PP (see grey bars in Figure S4, Supporting Information), namely the stretching modes of CH , CH_2 , and CH_3 in the range $2850\text{--}2950 \text{ cm}^{-1}$, the $\rho(\text{CH}_2)$, $\nu(\text{CC})$, $\nu(\text{C-CH}_3)$, and $\rho(\text{CH}_3)$ at 846 cm^{-1} , the $\rho(\text{CH}_2)$, $\nu(\text{CC})$, and $\nu(\text{C-CH}_3)$ at 808 cm^{-1} , and the $\varpi(\text{CH}_2)$ at 454 cm^{-1} .

3.2. Coating Metallic NPs onto PP and PP/MWCNT4% Filaments

The metallic NPs (Ag NPs and Au NPs)-coated filaments (PP and PP4%) were prepared via in situ approach using the citrate reduction method.^[10,38,46] This one-step approach originates parti-

cle aggregation and good homogeneity of the metallic NPs on the surface of the filament that will be vital to improving the final properties of the material. The first evidence of the presence of Ag NPs or Au NPs in the filament samples is the yellow and purple color observed in the Ag/PP, Ag/PP4% and Au/PP, and Au/PP4%, respectively (Figure S5, Supporting Information). It should be noticed that bigger aggregates of Au NPs can be seen by the naked eye for Au/PP filaments (big purple spots).

Figure S6A, Supporting Information, illustrates the visible spectra of PP and PP4% coated with Ag and Au NPs and the respective metal colloids together with the corresponding TEM images (Figure S6B, Supporting Information). The visible absorption spectrum for the colloidal Ag NPs prepared by the citrate reduction method has a single band at 446 nm ascribed to the localized surface Plasmon resonance (LSPR) band of such particles (Figure S6B—top, Supporting Information). The TEM image of the Ag colloid presented a polydisperse sample with spheroidal particles of $\approx 80 \text{ nm}$ in diameter. The optical spectra of the Ag/PP and Ag/PP4% filaments clearly show the LSPR for Ag NPs at 406 and 395 nm , respectively (Figure S6A—top, Supporting Information). The optical spectra of neat PP and PP4% filaments are also shown for comparison. The broad and shifts for the LSPR band on the Ag/PP and Ag/PP4% are expected due to small changes in the dielectric surroundings, interparticle Plasmon coupling, and possible particle aggregation.

The UV-VIS spectrum of Au NPs shows a LSPR at 516 nm , consistent with particles with 15 nm of diameter (Figure S6B—bottom, Supporting Information). Both optical spectra for Au/PP and Au/PP4% present the LSPR for Au NPs at 568 and 462 nm , respectively. The broad band observed for Au/PP4% indicates a polydisperse Au NPs on the filament surface, while the redshift of the LSPR band for Au/PP filaments can be correlated to the presence of Au aggregates on the filament surface (Figure S6A—bottom, Supporting Information). The latter observation is in line with the digital photograph presented in Figure S5e, Supporting Information, and can be explained by the method used to fabricate the Au/PP filaments. In the in situ method, the Au NPs are prepared by the reduction of an Au(III) precursor in the presence of the PP filaments, in which the impurities on the surface of the polymeric matrix observed in the AFM topography image (Figure S3a, Supporting Information) can promote the formation of particle aggregation.

The XRD patterns of neat PP, PP4% filaments, and metal NPs-loaded PP and PP4% composites are presented in Figure S6C, Supporting Information. PP shows a single phase α with peaks at 25.6° (060) and 28.9° (220). The reinforcement with 4% wt of MWCNT does not show substantive variations concerning the XRD results of PP, which is indicative that MWCNTs do not contribute to the formation of other PP phases.^[47]

Regarding metal NPs-loaded PP and PP4% composites, XRD patterns show typical diffraction peaks of PP in the range of $25\text{--}30^\circ$, demonstrating that no significant changes in crystallinity occur by the filaments' coating with Ag NPs or Au NPs. In the diffractograms of metal NPs-loaded PP and PP4% composites, two additional peaks are assigned to the (111) and (200) planes of Ag NPs and Au NPs, both face-centered cubic structures (JCPDS Card No. 04-0784).^[16]

Figure 2 shows SEM images acquired in SE and BSE modes, respectively, of metal NPs-loaded PP and PP4% filaments. While

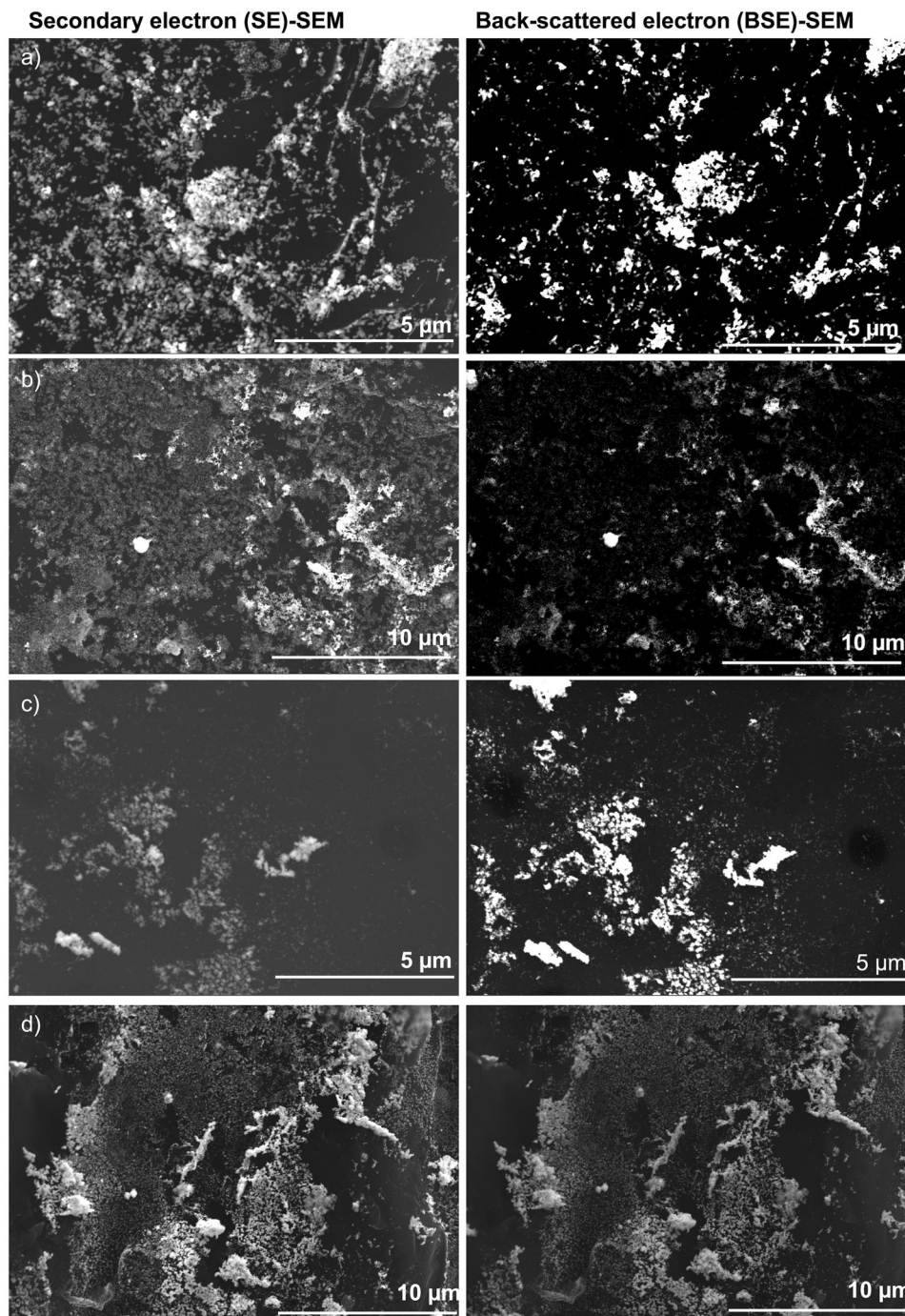


Figure 2. SEM images in SE (left) and BSE (right) modes of A) Ag/PP, B) Ag/PP4%, C) Au/PP, and D) Au/PP4%.

the SE mode provides an image with topographic contrast, the BSE mode originates an image with atomic weight contrast. Thus, the images in BSE mode mostly show the metallic NPs (Ag or Au NPs), as confirmed by EDS mapping analysis (**Figure 3**).

It is clear that the smooth surfaces of the neat PP and PP4% filaments turn into surfaces with higher roughness after attaching the metallic NPs, leading to regions enriched in metallic NPs distributed over the filament's surface. A careful look at the par-

ticles' size and morphology indicates that the Ag NPs have a spheroidal morphology, in which rods and triangle-shaped particles can also be observed (**Figure 3A[b]**). The Au/PP filament shows fewer Au NPs and more agglomerates than Au/PP4% (**Figure 2C,D**).

AFM was also used to assess differences in the surface properties of the metal NPs-loaded PP4% filaments and metal particle size. The topographic profile was recorded to verify the size

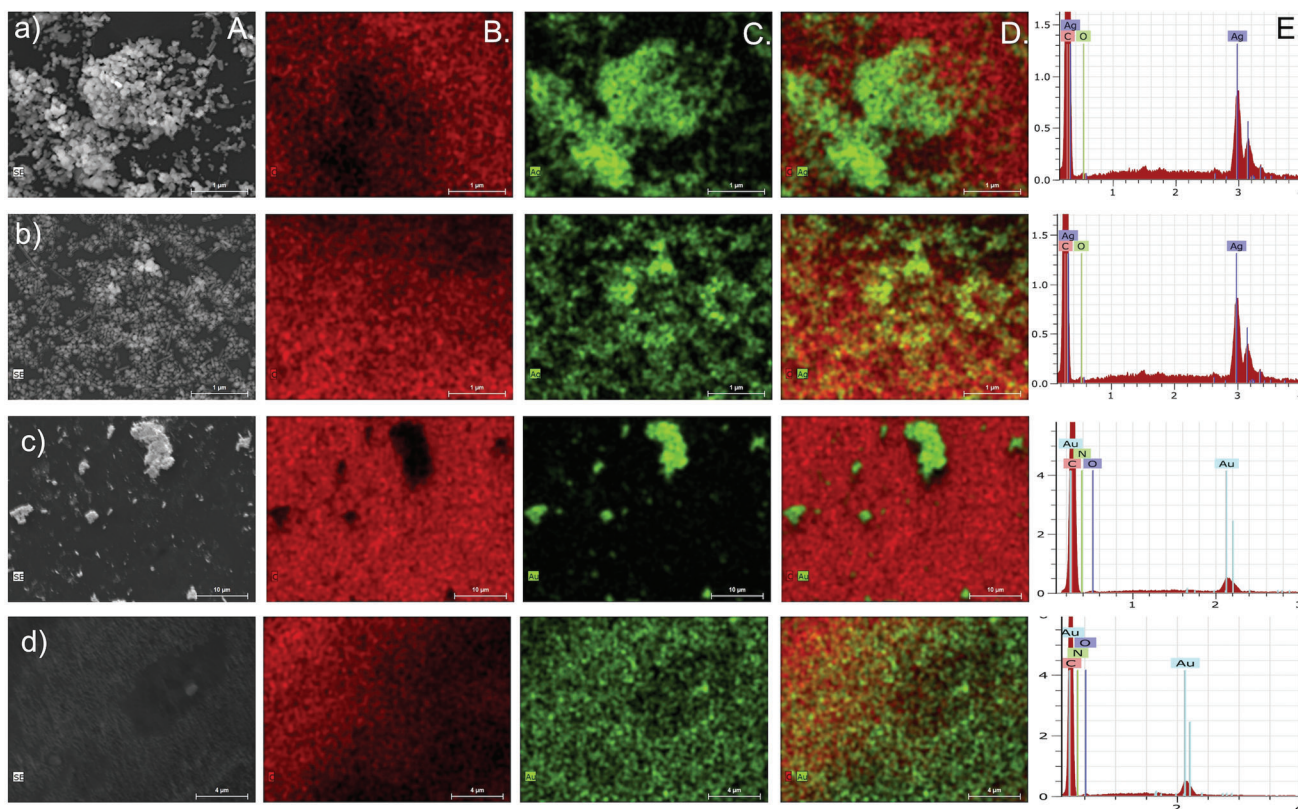


Figure 3. A) SEM image, B–D) EDS mapping (carbon [red] and silver or gold [green]), and EDS analysis E) of Ag/PP (a), Ag/PP4% (b), Au/PP (c), and Au/PP4% (d).

of the metallic NPs (Figure S7, Supporting Information), which was found to be between 80 and 100 nm for Ag/PP4% and 20 and 50 nm for Au/PP4%. The RMS values for Ag/PP4% filaments were 45.7 nm, while for the Au/PP4%, RMS values were higher (72.2 nm). This could be explained by the smaller size of the AuNPs, which can lead to more roughness on the filament surface.

The amount of metal in the filaments was evaluated by ICP, giving typical values of about 1010 and 988 mg kg⁻¹ for Ag/PP and Ag/PP4%, respectively, and 335 and 1555 mg kg⁻¹ for Au/PP and Au/PP4% (Table 2). The difference observed for Au NPs in the PP filaments could be justified by the particle aggregation observed in both the UV-VIS spectrum and SEM images.

3.3. SERS Performance of Metal NPs-Loaded PP and PP4% Filaments

Discharging industrial dyes in water supplies is a matter of concern, and their efficient detection and removal is an open challenge.^[48] MB is a cationic dye widely used for dyeing textiles and wood, and it produces potentially carcinogenic aromatic amines such as benzidine and methylene.^[48,49] Due to its high SERS activity, MB was used as a molecular probe to assess and optimize the SERS performance of metal NPs-loaded PP and PP4% filaments. A drop of an aqueous solution of MB (10 μM; 10 μL) was placed on the surface of the filament (Figure S8A, Supporting

Information), and then the substrate surface was analyzed by Raman spectroscopy. Figure 4A shows the average Raman spectra of MB (10 μM) adsorbed on the filament substrates. First, it is observed that the SERS spectra in Figure 4A[c–g] are similar to the conventional Raman spectra of a MB aqueous solution (0.1 M, presented in Figure 4A[a]). Control experiments recording the Raman spectrum of aqueous solutions with the same concentration of MB (10 μM) did not give Raman signal (data not shown). The conventional Raman spectra of all filaments (without MB) and the assignment of the Raman bands of MB according to the literature are presented in Figure S8B and Table S2, Supporting Information,^[50,51] respectively.

Second, while the Raman analysis on neat PP filaments (i.e., without metallic NPs) did not show the Raman signal of MB (Figure 4A[b]), the Raman spectrum of MB adsorbed on PP4% filament shows the characteristic Raman bands of the MB; however, lower as compared to PP4% coated with metallic NPs (Figure 4A[e]). One possible explanation for this result is the formation of π - π interactions between the carbon hexagonal rings present on CNTs with the aromatic rings of MB, promoting better adsorption of MB and, consequently, its detection.^[52] This agrees with the literature about using CNTs as SERS platforms to detect organic molecules.^[52,53]

Third, an enhancement of the Raman signal for MB is observed when adsorbed on PP filaments and PP4% filaments, both coated with metallic NPs due to the presence of metallic fillers on the filaments' surface.

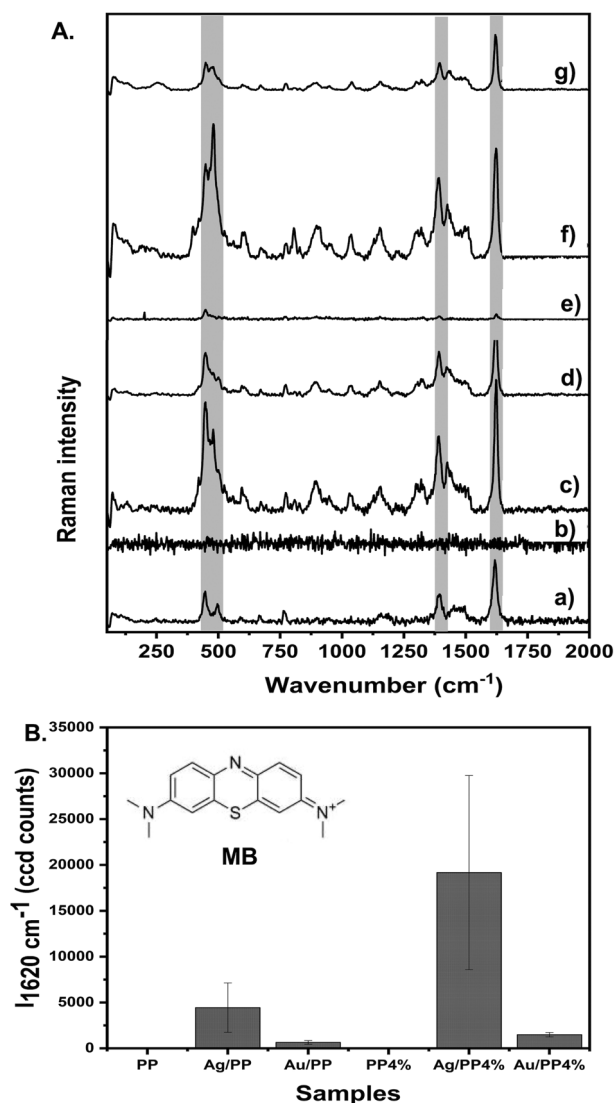


Figure 4. A) Conventional Raman spectrum of MB aqueous solution 0.1 M (a). SERS spectrum of MB (10 μm) obtained by the average of ten Raman spectra collected in different spots of PP (b), Ag/PP (c), Au/PP (d), PP4% (e), Ag/PP4% (f), and Au/PP4% (g) (excitation 633 nm, 0.1 mW laser power, and ten acquisitions of 2 s). B) Plot of the average Raman intensity of the band 1620 cm⁻¹ in the SERS spectrum of MB (10 μm) for PP, Ag/PP, Au/PP, PP4%, Ag/PP4%, and Au/PP4%. The inset shows the molecular structure of MB.

Figure 3B shows a comparative plot between the SERS intensity of the MB and the PP composite filaments used. For each PP composite filament, the intensity of the MB Raman band at 1620 cm⁻¹ (assigned to the $\nu(\text{CC}) + \delta(\text{CH})$ in plane (ring), $\nu(\text{CN}) + \nu(\text{CC})$) was calculated using Gaussian function and used to construct Figure 3B. Note that the metal NPs-loaded PP4% filaments show better selectivity for MB than their counterpart (metal NPs-loaded PP without MWCNT). It is known that the loading of metallic NPs on carbon materials, such as CNTs, can result in highly active SERS substrates due to the conjugation of the strong local electromagnetic field in the metallic NPs and the chemical mechanism from carbonaceous material.^[54]

This synergistic interaction induces different plasmonic effects from either the metal or the graphene layers of the CNT due to the charge transfer between them and the target molecule, enhancing the SERS enhancement factor to another order of magnitude.

This result also indicates that the substrate containing Ag NPs and MWCNTs presents the best SERS activity among the substrates tested; thus, in the adsorption experiments, the 3D-printed lattices loaded with Ag NPs and MWCNTs have been preferentially used.

The distribution of the MB molecules was accessed by SERS imaging. Figure 5 shows the SERS images for the Ag/PP4% and Au/PP4% filaments used as sensors. The SERS images were obtained by integrating the Raman band's area of MB at 1620 cm⁻¹. The brighter areas match the regions with stronger Raman signals for MB molecules adsorbed on the metallic particles distributed over the PP4% filaments, showing regions of higher intensity in specific filament areas related to the presence of metallic NPs. The position of the metallic NPs in the filament can also be monitored by SERS imaging, considering that a higher MB SERS signal can only be obtained when the molecular probe is adsorbed on the metal surface. However, the Raman signal for MB using Au/PP4% is lower than Ag/PP4% filament (Figure 4B); the SERS image presented in Figure 5D demonstrates a good homogenous and dense distribution of the Au NPs on the filament surface.

3.4. Uptake and SERS Detection of MB Using 3D Printed Lattices

It is highly desirable to develop efficient macro-structured adsorbents for industrial-scale implementation that can be easily handled and inexpensive. In this context, FFF-enabled macro-structured adsorbents comprising micrometer-sized orderly pores were realized. These micro-architected macro-structured adsorbents possess excellent surface area density (7.5 mm² mm⁻³, see Table 1) and therefore promote efficient mass transfer. As a proof of concept, the 3D printed geometries with non-porous and porous geometries (periodic cellular architecture with a porous size of 0.73 mm) fabricated using PP4% filaments were coated with Ag NPs to uptake MB molecules from water samples and detect them by SERS.

The 3D printed lattices coated with Ag NPs via in situ method (3D_Ag/PP4%cell and 3D_Ag/PP4%non) were analyzed by electron microscopy, and their SEM images are presented in Figure 6A,B. Both 3D printed lattices processed using the filaments with Ag NPs on their surface show more agglomeration in the periodic cellular geometry. In this coating process, the Ag⁺ cations are first reduced to Ag⁰ atoms, then the Ag⁰ atoms are assembled into Ag NPs. As the Ag NPs form, they aggregate due to their high affinity with each other at the 3D printed lattices' surface.^[10,55] The Ag⁺ cations' reduction can occur at the MWCNTs' surface (aromatic rings and functional groups (COO⁻)) or on the defects present on the PP matrix, onto which the cations can coordinate.

The amount of Ag in the 3D printed lattices was evaluated by ICP, giving typical values of about 488 and 535 mg kg⁻¹ for 3D_Ag/PP4%cell and 3D_Ag/PP4%non, respectively (Table 2). The decrease of Ag amount in the 3D lattices when compared

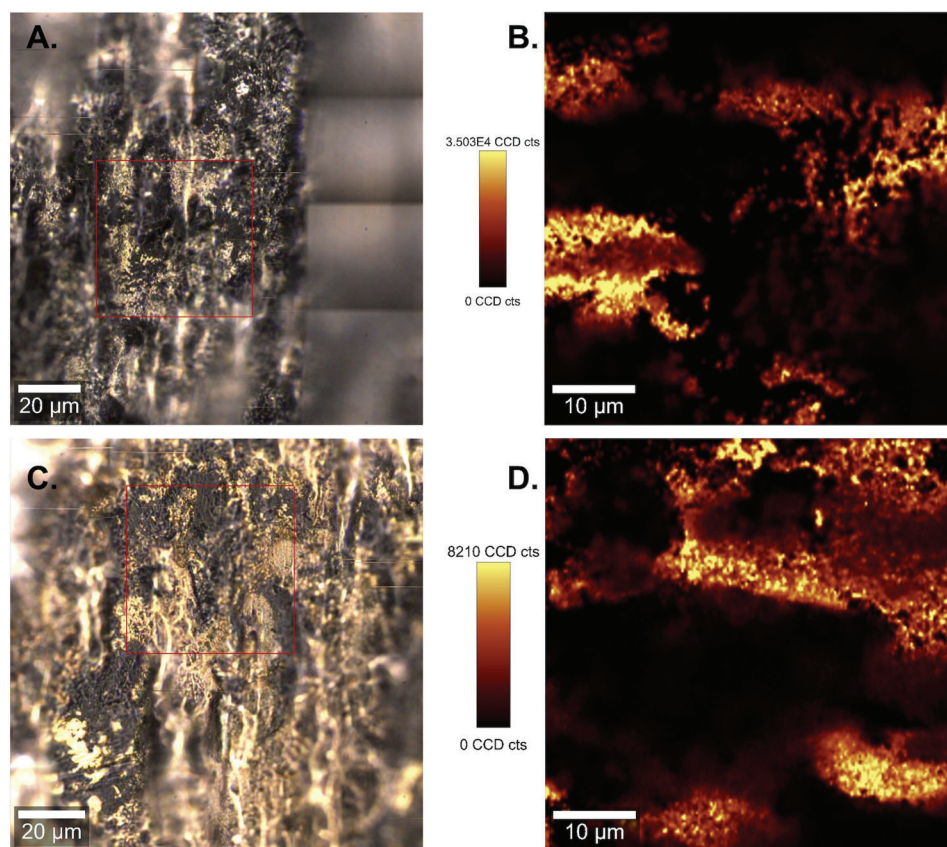


Figure 5. A) Optical images of Ag/PP4% and C) Au/PP4% with the scan area marked in red and the respective SERS images obtained with the integrated intensity of the band at 1620 cm^{-1} in the SERS spectra of MB $10\text{ }\mu\text{m}$ recorded using B) Ag/PP4% and D) Au/PP4% as substrates (excitation at 633 nm , 0.1 mW laser power). The vertical bar shows the color profile in each image, with the relative intensity scale.

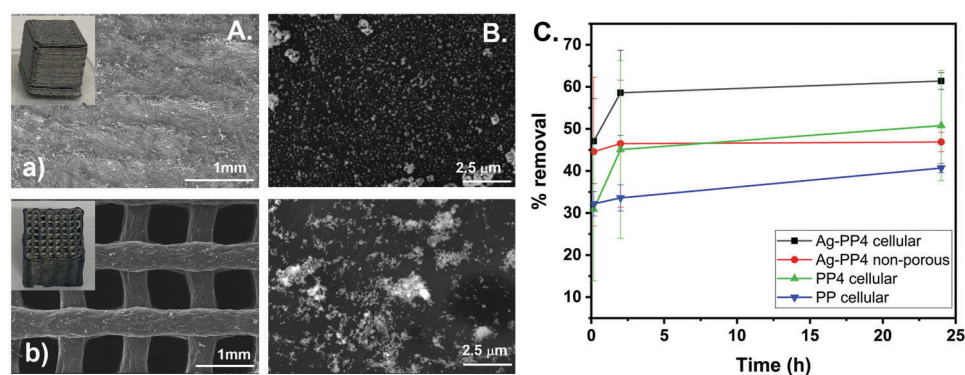


Figure 6. A) SEM images and B) high-magnification SEM images of 3D_Ag/PP4%non (a) and 3D_Ag/PP4%cell (b) structures; Inset: Digital photographs of Ag-coated 3D printed lattice samples. C) Removal percentage of MB ($10\text{ }\mu\text{m}$, $20\text{ }^\circ\text{C}$, $\text{pH } 9$) for 3D_Ag/PP4%cell (red circle), 3D_Ag/PP4%non (black square), 3D_PP4%cell (green triangle), and 3D_PPcell (blue inverted triangle).

with filaments can be explained by the 3D printing process that can reduce the roughness surface of the material, creating fewer spots for particle growth.

The adsorption process of MB aqueous solution is dependent on the pH, being more favorable at alkaline pH values, regardless of the sorbent nature.^[51,56–58] For CNTs as sorbent materials,

the MB removal capacity appears optimal at pH values between 9 and 10.^[51] Thus, the adsorption behavior of the 3D printed lattice reported here was investigated at pH 9.

Figure 6C shows the removal percentage of MB ($10\text{ }\mu\text{m}$, $20\text{ }^\circ\text{C}$, $\text{pH } 9$) for 3D_Ag/PP4%cell, 3D_Ag/PP4%non, 3D_PP4%cell, and 3D_PPcell scaffolds. Control experiments carried out in

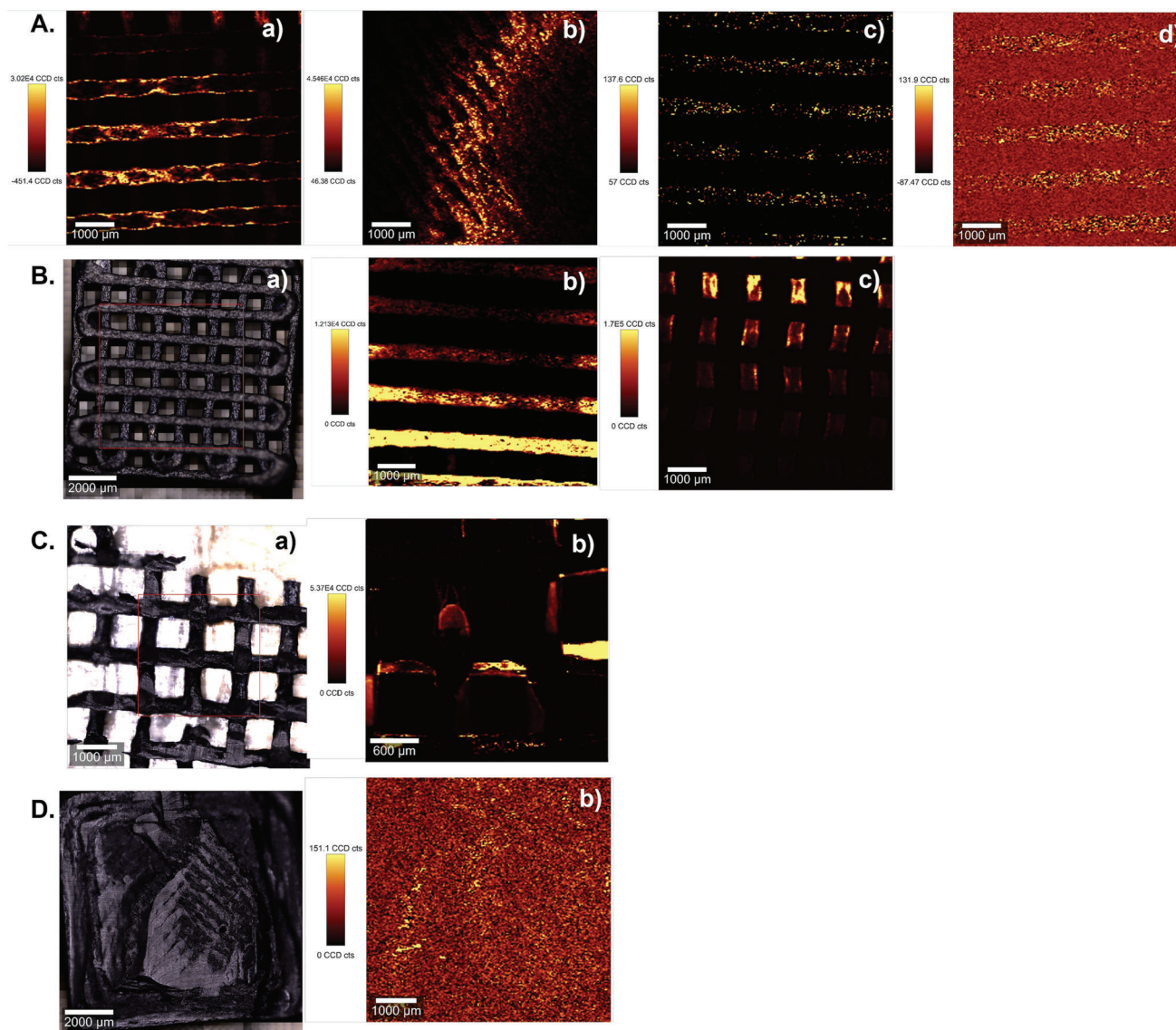


Figure 7. A) SERS images obtained with the integrated intensity of the band at 1620 cm^{-1} in the SERS spectra of MB $10\text{ }\mu\text{m}$ adsorbed on 3D_Ag/PP4%cell (a) 3D_Ag/PP4%non (b), 3D_PP4%cell (c), and 3D_PPcell (d) (excitation at 633 nm , 0.1 mW laser power). B) Optical image (a) and in-depth Raman images obtained using the integrated intensity of the Raman band at 1620 cm^{-1} in the SERS spectra of MB $10\text{ }\mu\text{m}$ using the 3D_Ag/PP4%cell for $0\text{ }\mu\text{m}$ (b) and $-350\text{ }\mu\text{m}$ (c). C) Optical image (a) and Raman image of MB $10\text{ }\mu\text{m}$ (1620 cm^{-1}) adsorbed in the 3D_Ag/PP4%cell cross section (b). D) Optical image (a) and Raman image of MB $10\text{ }\mu\text{m}$ (1620 cm^{-1}) adsorbed in the 3D_Ag/PP4%non cross section (b). The vertical bar on the right shows the color profile and the relative intensity scale.

parallel in the absence of sorbent lattices under the same pH conditions and contact time have demonstrated no losses of MB (data not shown). The optical measurements for one replica for each 3D printed lattice are illustrated in Figure S9, Supporting Information. Note that the 3D_Ag/PP4%cell structure has a higher adsorption capacity (61%) after 24 h than the 3D printed lattice structures without Ag NPs (3D_PP4% [51%] and 3D_PP [41%]). These results suggest that the adsorption of MB increases due to the presence of the Ag NPs at the surface of the 3D printed lattices. These results suggest that the adsorption of MB increases due to the presence of the Ag NPs at the surface of the 3D printed lattices. The adsorption of the MB molecules

on the Ag NPs surface occurs through electrostatic interactions between the negative charge of the Ag NPs' citrate coating and the positive charge of the MB molecules.^[47]

Concerning the structure of the 3D printed samples as sorbents, the non-porous geometry presents lower adsorption (47%) than the porous architecture (61%). This result demonstrates that the architecture of the adsorbent plays a crucial role in the adsorption process, and the lattice geometry employed here offers significantly enhanced surface area density ($7.5\text{ mm}^2\text{ mm}^{-3}$, Table 1) compared to non-porous geometry ($0.6\text{ mm}^2\text{ mm}^{-3}$), enabling reduction in diffusion time and improvement in dye transfer efficiency. Dong et al. have already reported this

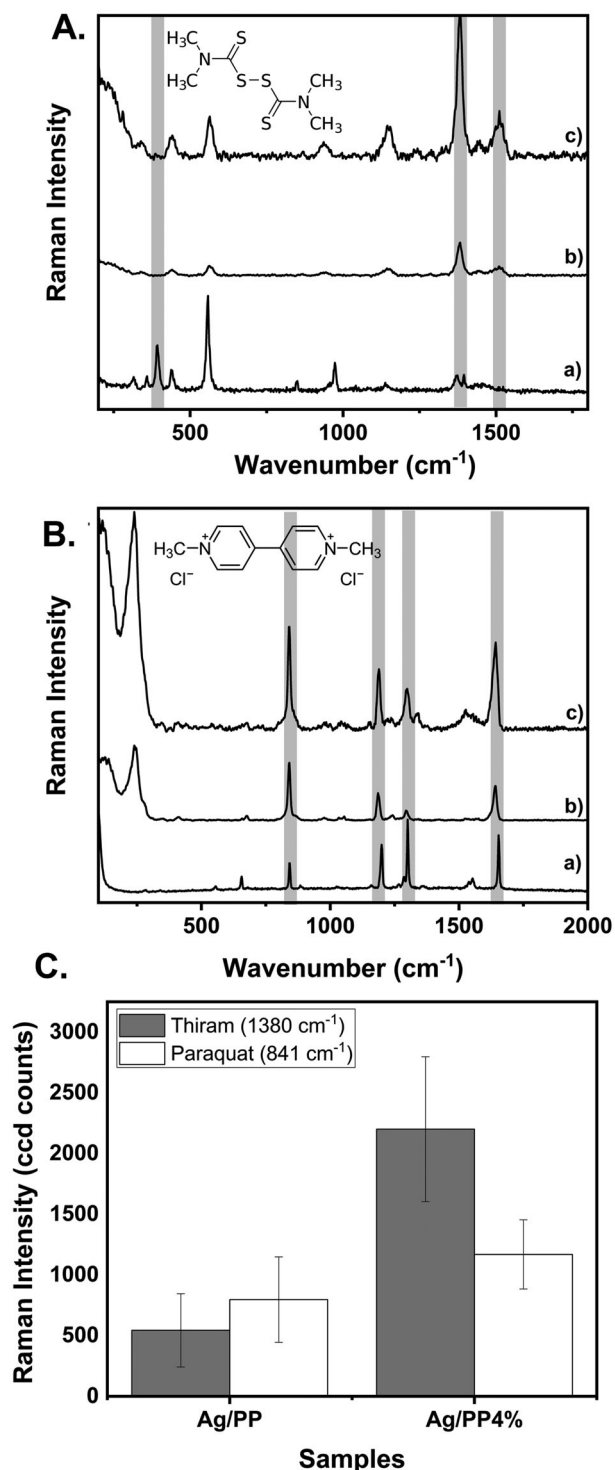


Figure 8. Raman spectra (excitation at 633 nm, 0.1 mW laser power, ten scans with 2 s acquisition time each) of A) thiram and B) paraquat for the powders (a), and respective average SERS spectra (10 μm) using Ag/PP (b) and Ag/PP4% (c) filaments. Inset: Molecular structure of thiram (top) and paraquat (down). C) Plot of the intensity of specific SERS bands of thiram (1380 cm^{-1}) e paraquat (841 cm^{-1}) using the Ag/PP and Ag/PP4% filaments.

adsorption behavior for 3D printed dimethyl aminoethyl methacrylate hierarchically porous scaffolds.^[59] In addition, all samples with MWCNT demonstrate rapid adsorption at the beginning, that is, for short contact times with the sorbent. This can be explained by the planar structure of MB that will interact with the CNTs through π - π interactions.^[51] The specific surface area of 3D printed lattice structures was also investigated by the N_2 sorption/desorption technique (Table S3, Supporting Information). The 3D neat PP lattice displays a small specific surface area of 2.5 $\text{m}^2 \text{g}^{-1}$. The specific surface area of the PP lattice decreased to 0.73 $\text{m}^2 \text{g}^{-1}$ after being reinforced with MWCNTs. However, the incorporation of Ag NPs substantially enhances the specific surface area: 13.9 $\text{m}^2 \text{g}^{-1}$ for the cellular structure and 3.12 $\text{m}^2 \text{g}^{-1}$ for the non-porous structure.

After 24 h in contact with an aqueous solution of MB (10 μM , 20 $^\circ\text{C}$, pH 9), the 3D samples were analyzed by SERS imaging, and the results are presented in Figure 7. The large-SERS images using 40 000 spectra by raster-scanning the laser beam over a surface area of 6 \times 6 mm show that even all the 3D printed samples demonstrate adsorption of MB, only the sorbents with Ag NPs show SERS activity to detect the MB molecules (Figure 7A[a,b]). Note that the SERS image acquired on the 3D sample printed with PP4% filaments shows the presence of MB molecules; however, the Raman signal is very weak compared to the 3D cubic samples coated with Ag NPs.

It is crucial to evaluate the in-depth dispersion of the Ag NPs in the 3D cubic sample to obtain information about the metallic NPs distribution throughout the 3D-printed sample (surface and interior) and its performance as an adsorbent. Thus, SERS images of 3D_Ag/PP4%cell after being in contact for 24 h with an aqueous solution of MB (10 μM , 20 $^\circ\text{C}$, pH 9) were built along the z-direction (down to -350 μm) (Figure 7B[a-c]). Figure 7B[b] shows the MB molecules dispersed on the surface of the filaments horizontally aligned (surface of the substrate, $z = 0 \mu\text{m}$). Down to -350 μm , the Raman signal of MB is also detected in the filaments vertically aligned with the surface ones (Figure 7B[c]). This result confirms the homogeneous distribution of Ag NPs in the two overlapping filaments on the surface, reinforcing that the periodic cellular structure has a higher surface area to adsorb water pollutants.

Then, the 3D_Ag/PP4%cell was cut in the middle and analyzed by SERS imaging. Figure 7C shows the presence of MB all over the filaments. This means that the Ag NPs are well distributed all over the 3D cubic periodic cellular sample, including on the inside, increasing its capability to adsorb the MB molecules. This observation can be explained by the synthesis method used to prepare the Ag NPs. In the citrate reduction method, the cationic silver ions are diffused into the cubic cellular structure interior, allowing nucleation and growth of Ag NPs in the filament's surface located inside the cellular structure.

On the contrary, the interior of the 3D_Ag/PP4% non-structure is less active in detecting MB (see bright spots in Figure 7D[b]) due to the absence of Ag NPs in the interior filaments. The observed Raman signal of MB can be explained by the diffusion of the MB molecules through the cubic structure that contains small gaps between the filaments (see Raman imaging in Figure 7A[b]). Here, the MB molecules are adsorbed on the MWCNT present on the filaments' surface, as demonstrated by the SERS spectrum in Figure 4A[e].

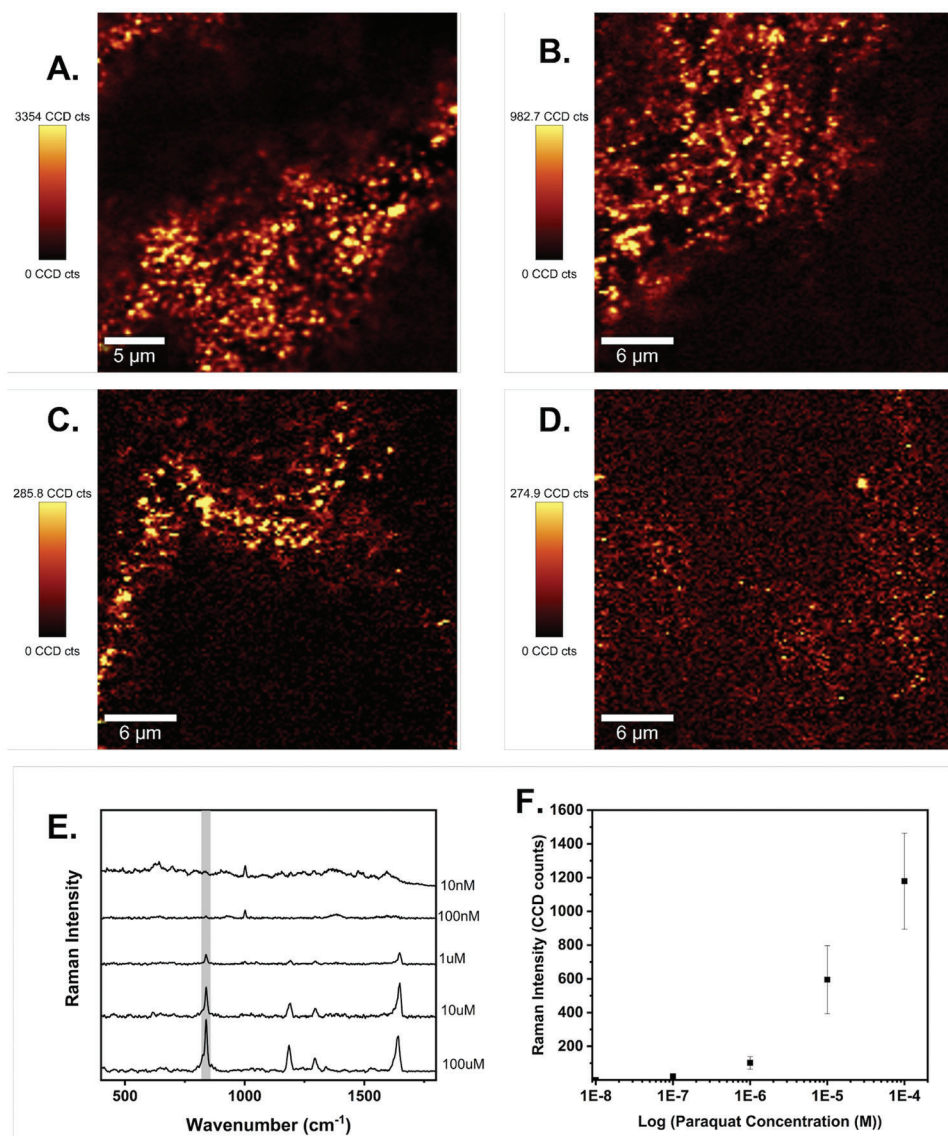


Figure 9. Raman images obtained with the integrated intensity of the band at 841 cm^{-1} of paraquat recorded using Ag/PP4% filament as SERS sensor for samples of paraquat with variable concentrations: A) $100\text{ }\mu\text{M}$; B) $10\text{ }\mu\text{M}$; C) $1\text{ }\mu\text{M}$; D) 100 nM . The vertical bar shows the color profile in each image, with the relative intensity scale. E) Average of ten SERS spectra of paraquat molecules taken from the Raman images in ultrapure water with variable paraquat concentrations. F) Plots of the intensity of the 841 cm^{-1} paraquat Raman band for varying paraquat concentrations, using three different samples (Ag/PP4%) for each concentration.

3.5. SERS Detection of Pesticides Using Ag/PP and Ag/PP4% Filaments

The Ag/PP and Ag/PP4% filaments were evaluated as SERS sensors to detect pesticides, namely, thiram (a fungicide used in seed and crops to prevent fungal diseases) and paraquat (a herbicide used for weed control). In this experiment, $10\text{ }\mu\text{L}$ of a pesticide solution ($100\text{ }\mu\text{M}$) in ultrapure water was dropped on the Ag/PP and Ag/PP4% filaments, and after drying, the SERS analysis was performed. The experimental Raman bands of thiram and paraquat and respective vibrational mode assignments are presented in Table S2, Supporting Information.^[10,60–64] The SERS spectra for thiram and paraquat aqueous solutions, using both Ag/PP and Ag/PP4% filaments, are presented in Figure 8A,B. The conven-

tional Raman spectrum of thiram and paraquat powder is also shown in Figure 8A[a],B[a] for comparative purposes.

In Figure 8, the Ag-coated PP filaments can detect the pesticide molecules regardless of the presence or not of MWCNTs in the filaments. However, the Ag/PP4% filament exhibits higher Raman sensitivity for thiram and paraquat than Ag/PP (Figure 8C), which is in line with the observations for MB molecules.

Several changes are evident in the SERS spectra of thiram (Figure 8A[b,c], grey bars) when compared to the conventional Raman spectrum of thiram powder (Figure 8A[a]). These observations result from the interaction between the thiram molecules and the Ag surface, which has been reported elsewhere.^[10,64] The most noticeable differences are the absence of the band at 389 cm^{-1} (molecular cleavage by breaking of the disulfide thiram

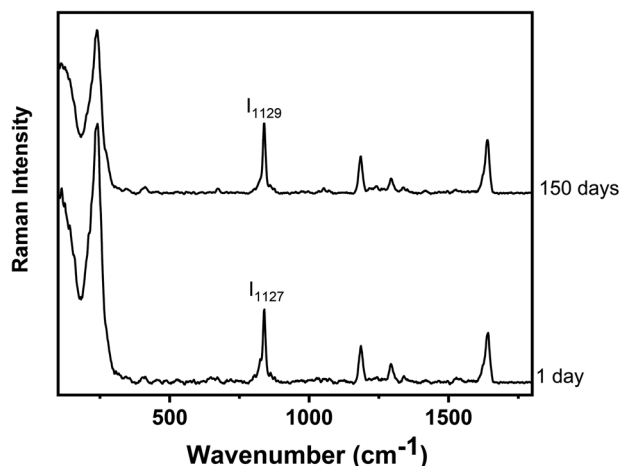


Figure 10. Average SERS spectra of paraquat (100 μM) on Ag/PP4% filament after 1 and 150 days of sensor storage. Each spectrum is the average of two different samples.

bond) and the enhancement of the Raman band at 1380 cm^{-1} assigned to the $\nu(\text{C-N})$ coupled to $\delta_{\text{sym}}(\text{CH}_3)$ (proximity of the methyl CH_3 and CN groups to the Ag surface). In addition, it is clear that the thiram molecules are adsorbed preferentially in a perpendicular orientation through the C-N bond with the Ag NPs (bidentate interaction) due to the absence of the band at 1452 cm^{-1} attributed $\delta_{\text{asym}}(\text{CH}_3)$ and the appearance of the band at 1498 cm^{-1} attributed to the $\nu(\text{C-N})$ in the SERS spectra.^[10,60,64]

In the SERS spectra of paraquat illustrated in Figure 8B[b,c], four strong characteristic Raman bands at 841, 1188, 1296, and

1639 cm^{-1} are observed. The strongest bands are at 1639 and 839 cm^{-1} assigned to the C=N stretching mode and C-N stretching mode, respectively.^[65,66] The enhancement of such bands is correlated to the adsorption of the paraquat molecules on the AgNPs surface through electrostatic interactions between the positively charged quaternary nitrogens present on the paraquat molecule and the negative charge surface of the AgNPs (zeta potential of $-52.7 \pm 1.29\text{ mV}$, $\text{pH } 7.23$).^[67]

To further evaluate the SERS sensitivity of Ag/PP4% filaments to detect thiram and paraquat, aqueous solutions with variable concentrations (100 μM –10 nM) of the analyte were prepared, and a 10 μL aliquot of the solution was placed onto the filament. **Figure 9** illustrates the Raman images obtained with the integrated intensity of the characteristic band of paraquat at 841 cm^{-1} using Ag/PP4% as SERS sensor. The SERS images show the spatial distribution of paraquat molecules on the Ag/PP4% filament using distinct paraquat concentrations. It should be highlighted that the Raman images obtained using low paraquat concentrations (Figure 9D) show small areas for the presence of the pesticide molecules, indicating the presence of few active Raman scattering sites in the Ag/PP4% filament (brighter colored areas).

The same procedure was used for thiram using the band at 1380 cm^{-1} as the diagnosis band (Figure S10, Supporting Information). Both the detection limit of paraquat and thiram in ultra-pure water was 100 nM . The average Raman spectra of paraquat e thiram obtained for the detection limits determination are presented in Figure 9E and Figure S10E, Supporting Information, respectively, and all characteristic Raman bands for thiram and paraquat were clearly observed in such diluted samples. Plots of the intensity of the Raman bands at 841 cm^{-1} for paraquat and

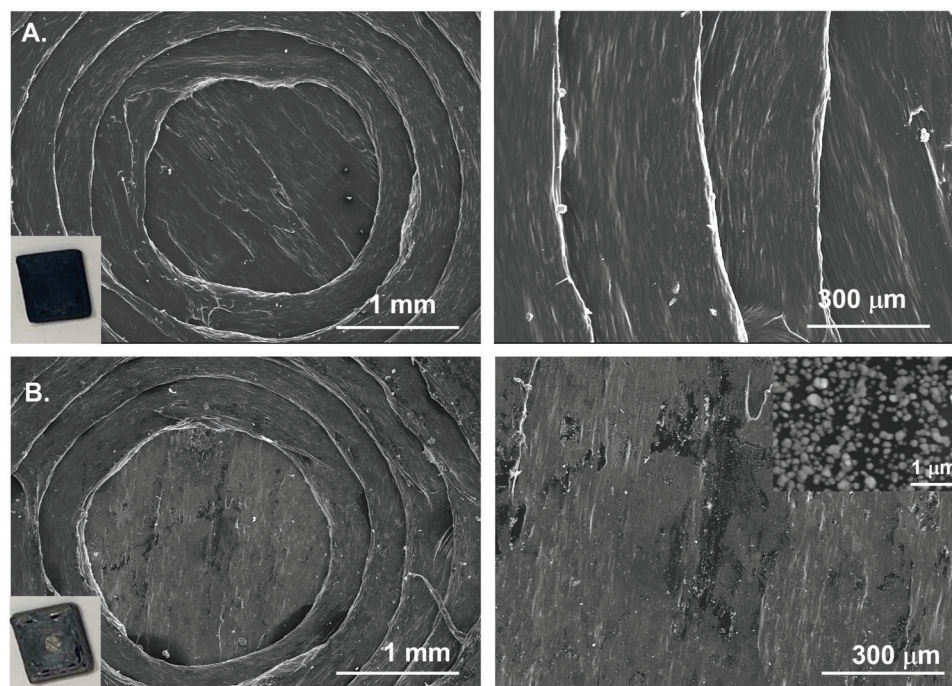


Figure 11. SEM images with different magnifications of A) PP4% and B) Ag/PP4% test strips. Insert image: PP4% (top) and Ag/PP4% (bottom) test strips.

1380 cm^{-1} for thiram for variable pesticide concentrations are also presented in Figure 9F and Figure S10F, Supporting Information.

The stability of a SERS sensor is crucial for practical detection applications. Therefore, the stability of Ag/PP4% filament over time was investigated. As shown in Figure 10, the two average spectra are very similar, with an increase of 0.1% for the paraquat band at 841 cm^{-1} over time. This result indicates good stability of Ag/PP4% filaments over 150 days of storage time.

3.6. SERS Detection of Paraquat in Spiked Real Water Samples Using a Portable Raman Spectrometer

A great advantage of AM technique is the possibility to create distinct structures with different shapes and morphologies using the same filaments. Thus, test strips with a cylindrically shaped recess ($8 \times 0.8 \times 0.8$ mm) were manufactured via FFF using PP4% and coated with Ag NPs to detect paraquat spiked in real water samples using a portable Raman spectrometer (Figure S11, Supporting Information).

PP4% and Ag/PP4% test strips were characterized by SEM analysis, as illustrated in Figure 11. In both samples, it can be clearly seen that the cylindrical shape recess of the 3D-printed structure and high-resolution SEM image on Ag/PP4% shows the presence of Ag NPs on its surface. It should be highlighted that there is a more concentration of Ag NPs in the middle of the test strip, maybe due to the printing process that can induce more growth spots for the AgNPs. This agglomeration of particles can be observed by the naked eye (insert image in Figure 11B).

As a proof-of-concept, the SERS detection of paraquat spiked in a complex water matrix using a portable Raman device was investigated for the Ag/PP4% test strips. Figure 12 details the SERS spectra recorded using Ag/PP4% test strips (785 nm, 5 mW) of paraquat spiked samples: A) distilled water, B) Aveiro Estuary water, and C) tap water with distinct concentrations. This result shows that Ag/PP4% test strip is sensitive for paraquat detection not only in complex water matrixes such as distilled water, Aveiro Estuary water, and tap water but also using a distinct laser source (785 nm). The average Raman spectra of paraquat molecules spiked in all complex water samples are similar to the Raman spectrum presented in Figure 8B, and the characteristic Raman bands of paraquat can be perfectly observed. In both cases, the detection limit achieved using such complex water matrices was equal to 1 μM . Although this value is higher than the detection limit for ultrapure water spiked with paraquat, using such 3D structures opens new perspectives and strategies to fabricate active SERS sensors to detect water pollutants in the field using portable devices.

4. Conclusions

In this study, we successfully fabricated low-cost architected hybrid sensors with high sensitivity and stability for the optical detection of water pollutants by combining the plasmonic properties of metallic NPs with AM-enabled nanocomposite lattice architectures. For the first time, 3D printed lattices coated with Ag NPs were used as sensors for the uptake and SERS detection

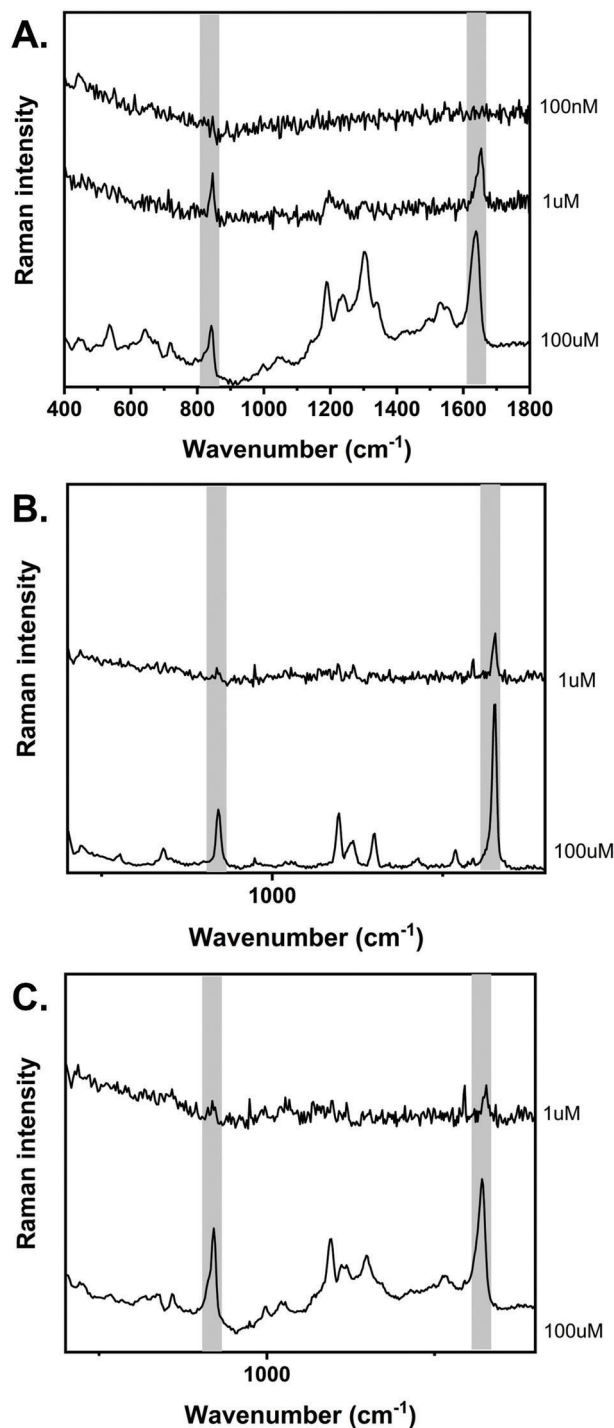


Figure 12. Average SERS spectra of spiked A) distilled water, B) Aveiro Estuary water, and C) tap water with distinct concentrations.

of MB. The 3D Ag/PP/4 wt%MWCNT lattice was demonstrated to be more efficient in capturing MB molecules than the 3D structures without Ag NPs (PP/4 wt%MWCNT). This improved efficiency is due to the strong affinity of the MB molecules to Ag NPs, namely through electrostatic interactions between the positive charge of MB molecules and the negative charge of the

metallic NPs' surface. In addition, the 3D printed lattice architecture also played a significant role in the adsorption behavior, due to its enhanced surface area density compared with that of non-porous geometry, reducing the diffuse time and improving the dye transfer efficiency. Raman imaging coupled with SERS methodology offered insights into the distribution of the Ag NPs on the entire surface of the 3D printed cellular and non-porous structures by monitoring the Raman signal of MB molecules.

Using a portable Raman spectrometer, a Raman test strip was fabricated with Ag/PP/4 wt%MWCNT to detect paraquat molecules spiked in real water matrices such as Aveiro Estuary water or tap water. The detection limit for paraquat in both real water samples was 1 μM , demonstrating that these hybrid sensors have great potential for on-site SERS water quality monitoring. We believe that the combination of AM-enabled cellular lattice architectures with plasmonic NPs opens a new field of research for developing hybrid sensors that can be used for sensing applications not only to detect water pollutants but also in other analytical contexts.

Supporting Information

Supporting Information is available from the Wiley Online Library or from the author.

Acknowledgements

This work was supported by the UK Engineering and Physical Sciences Research Council (grant EP/R513222/1), and the project CICECO-Aveiro Institute of Materials, UIDB/50011/2020, UIDP/50011/2020, and LA/P/0006/2020, financed by national funds through the FCT/MEC (PID-DAC). S.F. thanks FCT for her research contract (REF-069-88-ARH-2018), which is funded by national funds (OE) through FCT-Fundação para a Ciência e a Tecnologia, I.P., in the scope of the framework contract foreseen in the numbers 4, 5, and 6 of the article 23, of the Decree-Law 57/2016, of August 29, changed by Law 57/2017, of July 19. The authors additionally acknowledge the support given by the European Commission via the COST Action CA19118 "High-performance carbon-based composites with smart properties for advanced sensing applications" (EsSENce).

Conflict of Interest

The authors declare no conflict of interest.

Data Availability Statement

The data that support the findings of this study are available from the corresponding author upon reasonable request.

Keywords

additive manufacturing, architected materials, nanocomposites, surface-enhanced Raman scattering, water pollutants

Received: February 21, 2023
Revised: May 9, 2023
Published online:

- [1] M. Syafrudin, R. A. Kristanti, A. Yuniarto, T. Hadibarata, J. Rhee, W. A. Al-Onazi, T. S. Algarni, A. H. Almarri, A. M. Al-Mohaimed, *Int. J. Environ. Res. Public Health* **2021**, *60*, 125.
- [2] K. S. Rajmohan, R. Chandrasekaran, S. Varjani, *Indian J. Microbiol.* **2020**, *60*, 125.
- [3] M. Schleiffer, B. Speiser, *Environ. Pollut.* **2022**, *313*, 120116.
- [4] K.-H. Kim, E. Kabir, S. A. Jahan, *Sci. Total Environ.* **2017**, *575*, 525.
- [5] S. Rajput, A. Kumari, S. Arora, R. Kaur, *MethodsX* **2018**, *5*, 744.
- [6] H. C. Liang, N. Bilon, M. T. Hay, *Water Environ. Res.* **2015**, *87*, 1923.
- [7] M. C. Pablos-Espada, F. J. Arrebola-Liébanas, A. Garrido-Frenich, J. L. Martínez-Vidal, *Int. J. Environ. Anal. Chem.* **2006**, *75*, 165.
- [8] E. Benfenati, P. Tremolada, L. Chiappetta, R. Frassanito, G. Bassi, N. Di Toro, R. Fanelli, G. Stella, *Chemosphere* **1990**, *21*, 1411.
- [9] Z. Li, J. Wang, D. Li, *Appl. Spectrosc. Rev.* **2016**, *51*, 313.
- [10] S. Fateixa, M. Raposo, H. I. S. Nogueira, T. Trindade, *Talanta* **2018**, *182*, 558.
- [11] N. C. T. Martins, S. Fateixa, T. Fernandes, H. I. S. Nogueira, T. Trindade, *ACS Appl. Nano Mater.* **2021**, *4*, 4484.
- [12] Y. Yang, N. Creedon, A. O'Riordan, P. Lovera, *Photonics* **2021**, *8*, 568.
- [13] S. Pang, T. Yang, L. He, *TrAC, Trends Anal. Chem.* **2016**, *85*, 73.
- [14] S. Fateixa, H. I. S. Nogueira, T. Trindade, *Phys. Chem. Chem. Phys.* **2015**, *17*, 21046.
- [15] X. X. Han, R. S. Rodriguez, C. L. Haynes, Y. Ozaki, B. Zhao, *Nat. Rev. Methods Primers* **2022**, *1*, 87.
- [16] P. Pinheiro, S. Fateixa, H. Nogueira, T. Trindade, *Nanomaterials* **2019**, *9*, 31.
- [17] P. C. Pinheiro, S. Fateixa, A. L. Daniel-da-Silva, T. Trindade, *Sci. Rep.* **2019**, *9*, 19647.
- [18] S. Fateixa, H. I. S. Nogueira, T. Trindade, *ACS Omega* **2018**, *3*, 4331.
- [19] S. Jaitpal, S. R. Chavva, S. Mabbott, *ACS Omega* **2022**, *7*, 2850.
- [20] C. Garcia-Astrain, E. Lenzi, D. J. de Aberasturi, M. Henriksen-Lacey, M. R. Binelli, L. M. Liz-Marzán, *Adv. Funct. Mater.* **2020**, *30*, 2005407.
- [21] S. Almoammed, M. Alruwaili, E. G. Reynaud, G. Redmond, J. H. Rice, B. J. Rodriguez, *ACS Appl. Nano Mater.* **2019**, *2*, 5029.
- [22] A. Gebhardt, J.-S. Hötter, *Additive Manufacturing: 3D Printing for Prototyping and Manufacturing*, Hanser Publications, Munich, **2016**.
- [23] B. A. Praveena, N. Lokesh, A. Buradi, N. Santhosh, B. L. Praveena, R. Vignesh, *Mater. Today Proc.* **2022**, *52*, 1309.
- [24] J. Schneider, S. Kumar, *Polym. Test.* **2020**, *86*, 106357.
- [25] J. Ubaid, B. L. Wardle, S. Kumar, *Sci. Rep.* **2018**, *8*, 13592.
- [26] A. Mora, P. Verma, S. Kumar, *Composites, Part B* **2020**, *183*, 107600.
- [27] Sculpteo, *The State of 3D Printing Report: 2021 Edition*, Sculpteo, France, **2021**.
- [28] K. V. Wong, A. Hernandez, *ISRN Mech. Eng.* **2012**, *2012*, 1.
- [29] *Additive Manufacturing*, (Eds: A. Bandyopadhyay, S. Bose), CRC Press, Boca Raton, FL **2019**.
- [30] H. Bikas, P. Stavropoulos, G. Chryssolouris, *Int. J. Adv. Des. Manuf. Technol.* **2016**, *83*, 389.
- [31] V. Gupta, F. Alam, P. Verma, A. M. Kannan, S. Kumar, *J. Power Sources* **2021**, *494*, 229625.
- [32] F. Alam, K. M. Varadarajan, J. H. Koo, B. L. Wardle, S. Kumar, *Adv. Eng. Mater.* **2020**, *22*, 2000483.
- [33] P. Verma, J. Ubaid, K. M. Varadarajan, B. L. Wardle, S. Kumar, *ACS Appl. Mater. Interfaces* **2022**, *14*, 8361.
- [34] O. S. Carneiro, A. F. Silva, R. Gomes, *Mater. Des.* **2015**, *83*, 768.
- [35] M. Spoerk, J. Gonzalez-Gutierrez, C. Lichal, H. Cajner, G. Berger, S. Schuschnigg, L. Cardon, C. Holzer, *Polymers* **2018**, *10*, 490.
- [36] J. Ubaid, J. Schneider, V. S. Deshpande, B. L. Wardle, S. Kumar, *Adv. Eng. Mater.* **2022**, *24*, 2200194.
- [37] B. Adak, S. Mukhopadhyay, S. Kumar, in *Smart and Functional Textiles*, De Gruyter, Germany **2023**, pp. 683.
- [38] P. C. Lee, D. Meisel, *J. Phys. Chem.* **1982**, *86*, 3391.
- [39] R. L. McCreery, in *Raman Spectroscopy for Chemical Analysis*, John Wiley & Sons, New York **2005**, p. 49.

- [40] ISO (International Organisation for Standardisation), Determination of the specific surface area of solids by gas adsorption-BET method (ISO 9277), ISO, Geneva, Switzerland **2010**.
- [41] S. F. A. Acquah, B. E. Leonhardt, M. S. Nowotarski, J. M. Magi, K. A. Chambliss, T. E. S. Venzel, S. D. Delekar, L. A. Al-Hariri, S. F. A. Acquah, B. E. Leonhardt, M. S. Nowotarski, J. M. Magi, K. A. Chambliss, T. E. S. Venzel, S. D. Delekar, L. A. Al-Hariri, in *Carbon Nanotubes - Current Progress of their Polymer Composites*, IntechOpen, Rijeka **2016**, Ch. 8.
- [42] J. M. A. Alsharef, M. R. Taha, T. A. Khan, *J. Teknol.* **2017**, 79, 69.
- [43] E. Andreassen, in *Polypropylene*, Springer, Dordrecht **1999**, pp. 320–328.
- [44] N. Salah, A. M. Alfawzan, A. Saeed, A. Alshahrie, W. Allafi, *Sci. Rep.* **2019**, 9, 20288.
- [45] Y. Tong, Y. Lin, S. Wang, M. Song, *Polymer* **2015**, 73, 52.
- [46] I. V. Tudose, K. Mouratis, O. N. Ionescu, C. Romanitan, C. Pachiou, O. Tutunaru-Brincoveanu, M. P. Suche, E. Koudoumas, *Nanomaterials* **2022**, 12, 2411.
- [47] S. Fateixa, P. C. Pinheiro, H. I. S. Nogueira, T. Trindade, *J. Mol. Struct.* **2019**, 1185, 333.
- [48] S. Fateixa, M. Wilhelm, H. I. S. Nogueira, T. Trindade, *J. Raman Spectrosc.* **2016**, 47, 1239.
- [49] E. Fages, J. Pascual, O. Fenollar, D. García-Sanoguera, R. Balart, *Polym. Eng. Sci.* **2011**, 51, 804.
- [50] R. Al-Tohamy, S. S. Ali, F. Li, K. M. Okasha, Y. A.-G. Mahmoud, T. Elsamahy, H. Jiao, Y. Fu, J. Sun, *Ecotoxicol. Environ. Saf.* **2022**, 231, 113160.
- [51] A. M. Salgueiro, A. L. Daniel-da-Silva, A. V. Girão, P. C. Pinheiro, T. Trindade, *Chem. Eng. J.* **2013**, 229, 276.
- [52] X. Dong, H. Gu, J. Kang, X. Yuan, J. Wu, *Colloids Surf., A* **2010**, 368, 142.
- [53] G.-N. Xiao, S.-Q. Man, *Chem. Phys. Lett.* **2007**, 447, 305.
- [54] C. Xia, D. Zhang, H. Li, S. Li, H. Liu, L. Ding, X. Liu, M. Lyu, R. Li, J. Yang, Y. Li, *Nano Res.* **2022**, 15, 694.
- [55] J. A. Anastasopoulos, A. S. Beobide, L. Sygellou, S. N. Yannopoulos, G. A. Voyiatzis, *J. Raman Spectrosc.* **2014**, 45, 424.
- [56] X. Liang, N. Li, R. Zhang, P. Yin, C. Zhang, N. Yang, K. Liang, B. Kong, *NPG Asia Mater.* **2021**, 13, 8.
- [57] J. Ozhikandathil, S. Badilescu, M. Packirisamy, *Sci. Rep.* **2015**, 5, 13181.
- [58] S. Wang, Y. Boyjoo, A. Choueib, Z. H. Zhu, *Water Res.* **2005**, 39, 129.
- [59] S. F. Soares, T. R. Simões, T. Trindade, A. L. Daniel-Da-Silva, *Water, Air, Soil Pollut.* **2017**, 228, 87.
- [60] J. Ma, F. Yu, L. Zhou, L. Jin, M. Yang, J. Luan, Y. Tang, H. Fan, Z. Yuan, J. Chen, *ACS Appl. Mater. Interfaces* **2012**, 4, 5749.
- [61] D. Zhao, Y. Ding, S. Chen, T. Bai, Y. Ma, *Asian J. Chem.* **2013**, 25, 5756.
- [62] Z. Dong, H. Cui, H. Zhang, F. Wang, X. Zhan, F. Mayer, B. Nestler, M. Wegener, P. A. Levkin, *Nat. Commun.* **2021**, 12, 247.
- [63] S. Sánchez-Cortés, C. Domingo, J. v. García-Ramos, J. A. Aznárez, *Langmuir* **2001**, 17, 1157.
- [64] Y. Zhu, J. Wu, H. Gao, G. Liu, Z. Tian, J. Feng, L. Guo, J. Xie, *RSC Adv.* **2016**, 6, 59919.
- [65] H. Fang, X. Zhang, S. J. Zhang, L. Liu, Y. M. Zhao, H. J. Xu, *Sens. Actuators, B* **2015**, 213, 452.
- [66] M. Forster, R. B. Girling, R. E. Hester, *J. Raman Spectrosc.* **1982**, 12, 36.
- [67] S. Sánchez-Cortés, M. Vasina, O. Francioso, J. V. García-Ramos, *Vib. Spectrosc.* **1998**, 17, 133.
- [68] C. Zhu, D. Liu, M. Yan, G. Xu, H. Zhai, J. Luo, G. Wang, D. Jiang, Y. Yuan, *J. Colloid Interface Sci.* **2022**, 608, 2111.
- [69] R. Botta, P. Eiamchai, M. Horprathum, S. Limwichean, C. Chananonwathorn, V. Patthanasettakul, R. Maezono, A. Jomphoak, N. Nuntawong, *Sens. Actuators, B* **2020**, 304, 127327.
- [70] T. Fernandes, S. Fateixa, H. I. S. Nogueira, A. L. Daniel-Da-Silva, T. Trindade, *Eur. J. Inorg. Chem.* **2020**, 2020, 1153.